ANALOG VLSI IMPLEMENTATION OF RESONATE-AND-FIRE NEURON

KAZUKI NAKADA

Graduate School of Life Science and Systems Engineering,
Kyushu Institute of Technology,
2-4 Hibikino, Kitakyushu, Fukuoka 808-0196, Japan
nakada@brain.kyutech.ac.jp

TETSUYA ASAI

Graduate School of Information Science and Technology,
Hokkaido University Kita 14, Nishi 9,
Kita-ku, Sapporo, Hokkaido 060-0814, Japan

HATSUO HAYASHI

Graduate School of Life Science and Systems Engineering,
Kyushu Institute of Technology,
2-4 Hibikino, Kitakyushu, Fukuoka 808-0196, Japan

We propose an analog integrated circuit that implements a resonate-and-fire neuron (RFN) model based on the Lotka-Volterra (LV) system. The RFN model is a spiking neuron model that has second-order membrane dynamics, and thus exhibits fast damped subthreshold oscillation, resulting in the coincidence detection, frequency preference, and post-inhibitory rebound. The RFN circuit has been derived from the LV system to mimic such dynamical behavior of the RFN model. Through circuit simulations, we demonstrate that the RFN circuit can act as a coincidence detector and a band-pass filter at circuit level even in the presence of additive white noise and background random activity. These results show that our circuit is expected to be useful for very large-scale integration (VLSI) implementation of functional spiking neural networks.

Keywords: Analog integrated circuit; very large-scale integration (VLSI); spiking neural networks; resonate-and-fire Neuron (RFN) model; coincidence detection; frequency preference.

1. Introduction

Dynamical properties of spiking neural networks and their functional roles in information processing have been considered to be highly attractive from a point of view of hardware implementation of neuromorphic systems.[1] In fact, findings in neuroscience[3−14] have provided valuable insights into implementation of functional networks of silicon spiking neurons. Based on these findings, such networks of silicon spiking neurons can increase noise robustness and tolerance

in sensory coding[29,32,33] and reduce the influence of device deviation on their operation[29,31−34,40,41] in addition to the abilities of information processing including image processing,[18−23,28] auditory feature extraction,[24,25] onset detection,[29] and learning and memory.[30,31], and of sensori-motor integration.[16]

Recent research efforts for functional networks of silicon spiking neurons concentrate on real-time event-based computation,[25−30,46−48] whereas major previous works have been related with rate-based

computation.[17−24] Furthermore, this trend would be accelerated toward multi-chip system integration by rapid progress in the address-event representation (AER) protocol,[15] which is an asynchronous inter-chip communication protocol for reducing massively connections in very large-scale integration (VLSI) systems.

For designing of functional networks of silicon spiking neurons, a major requirement is the ability to extract meaningful information embedded in spike sequences. Temporal filtering properties are needed to extract the frequency of spike sequences, which carry information in the event-based computation as well as the rate-based computation. Coincidence or synchrony detection are considered to play essential roles in information processing in the event-based computation since fine temporal structure of spike sequences may be another carrier of information.

Such functions of the information selectivity in silicon spiking neural networks are limited by the performance of components of the networks: neuron and synaptic circuits. For instance, the Axon-Hillock circuit,[1] widely known as an electronic analogue of the integrate-and-fire neuron (IFN) model, can only act as a low-pass filter for a sequence of pulses. For increasing the information selectivity, spiking neuron circuits,[31,42−49] such as a low-power IFN circuit with frequency adaptation[31] and asynchronous chaotic spiking neuron circuits,[47,48] have been alternatively developed. These neuron circuits provide functions of synchrony detection and temporal filtering to the network circuits. Synaptic circuits can also increase the information selectivity of silicon spiking neural networks.[29,31,32,35−41] These synaptic circuits act as a nonlinear temporal filter by themselves. However, most of these circuits can work more effectively at network level. For instance, it is required to combine multiple synaptic circuits for constructing a spatio-temporal filter or a band-pass filter.

In this paper, we propose an analog integrated circuit that implements a resonate-and-fire neuron (RFN) model proposed by Izhikevich.[50] The RFN model is a spiking neuron model that has second-order membrane dynamics, and thus exhibits fast subthreshold oscillation, resulting in the coincidence detection, frequency preference, and post-inhibitory rebound. Such dynamic behavior was implemented as an analog integrated circuit using complementary metal-oxide-semiconductor (CMOS) technology. We will demonstrate that the RFN circuit can act as a coincidence detector and a band-pass filter at circuit level through circuit simulations using the simulation program with integrated circuit emphasis (SPICE). We will further investigate (i) the effects of white noise and (ii) background random activity on the performance of the signal detection; the coincidence detection and the frequency preference. Finally, we will consider (iii) the influence of device deviation on the circuit operation.

This paper is organized as follows. In Sec. 2, the dynamical behavior and the related functions of the RFN model are described. In Sec. 3, analog integrated circuit implementation of the RFN model is illustrated in detail. In Sec. 4, we will show the simulation results for the signal detection of the RFN circuit. The summary of the present research is given in Sec. 5.

2. Resonate-and-Fire Neuron (RFN) Model

We here describe a resonate-and-fire neuron (RFN) model proposed by Izhikevich.[50] The RFN model is a spiking neuron model with second-order membrane dynamics and a firing threshold. The dynamics of the RFN model are as follows:

$$\dot{x} = bx - wy + I \qquad (1)$$

$$\dot{y} = wx + by \qquad (2)$$

or given by an equivalent complex form:

$$\dot{z} = (b + iw)z + I \qquad (3)$$

where $z = x + iy$ is a complex state variable. The real and imaginary parts, x and y, are the current- and voltage-like state variables, respectively. The constants, b and w are parameters, and I is an external input. If the variable y exceeds a certain threshold a_{th}, the variable z is reset to an arbitrary value z_o, which describes activity-dependent after-spike reset. This model exhibits a damped subthreshold oscillation of membrane potential due to the second-order membrane dynamics. As a result, the RFN model is sensitive to the timing of stimuli.[50]

Figure 1 shows typical behavior of the RFN model in response to input pulses. In this case, we used the following parameters: $b = -0.1$, $w = 1$, $a_{\mathrm{th}} = i$, $z_o = -0.5 + i$, and the input pulses were given by: $I = i_{\max} \cdot (t/\tau)\exp(1 - t/\tau)$, where the time constant $\tau = 50\,\mathrm{ms}$, the maximal amplitude
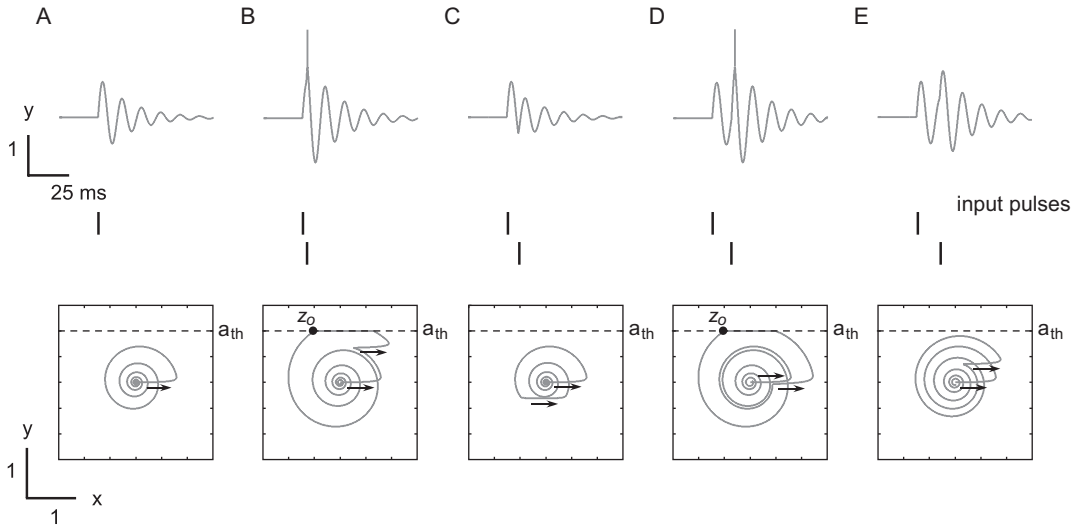
Fig. 1. Behavior of the resonate-and-fire neuron model in response to (A) a single pulse, (B) a coincident doublet, (C) a non-resonant doublet, (D) a resonant doublet, and (E) a non-resonant doublet. The output pulses are manually written to clarify the firing time in (B) and (D). Phase plane portraits show the sensitivity to the timing of the inputs, where the arrows represent the direction of the corresponding inputs.

$i_{\max} = 1.2$, and t was an elapsed time since a pulse was given. When a weak pulse that cannot evoke an action potential alone arrives at an RFN model, a damped subthreshold oscillation occurs, as shown in Fig. 1A. When a pair of pulses arrives at the RFN model at a short interval (a coincident doublet, e.g. 2.5 ms, Fig. 1B), or at an interval nearly equal to the intrinsic period of the subthreshold oscillation (a resonant doublet, 12.5 ms, Fig. 1D), the RFN model fires a spike. However, the RFN model does not fire a spike in response to a doublet with an interval in other ranges, e.g. 7.5 ms (Fig. 1C) or 15.0 ms (Fig. 1E).

These results indicate that the RFN model can detect coincidence pulses (coincidence detection), and resonate with a sequence of pulses at a resonance frequency (frequency preference). In addition it has been reported that the RFN model can fire a spike in response to an inhibitory pulse (post-inhibitory rebound).[50]

3. Circuit Implementation

We here propose an analog integrated circuit that implements the RFN model.[49] The circuit consists of a membrane circuit, a threshold-and-fire circuit, and excitatory and inhibitory synaptic circuits,[2,43] as shown in Fig. 2.

3.1. *Membrane circuit*

The membrane circuit was designed based on the Lotka-Volterra (LV) system having periodic solutions for mimicking the subthreshold membrane dynamics of the RFN model.[49]

3.1.1. *Lotka-Volterra (LV) system*

The LV system[53] is modeled after the interactions between multiple species in an ecological system, which is represented by the following equations:

$$\dot{z}_i = z_i \left(r_i + \sum_j^N a_{ij} z_j \right), \quad (i, j = 1, 2, \ldots, N) \qquad (4)$$

where N denotes the number of kinds of species Cz_i and r_i the population and the linear growth rate of the i-th species, respectively, and a_{ij} the interaction between the species. By introducing the nonlinear transformation:

$$z_i = b_i \exp x_i, \quad b_i = const. \qquad (5)$$

into the LV system, the following equation:

$$\dot{x}_i = r_i + \sum_j^N a_{ij} b_j \exp x_j, \qquad (6)$$

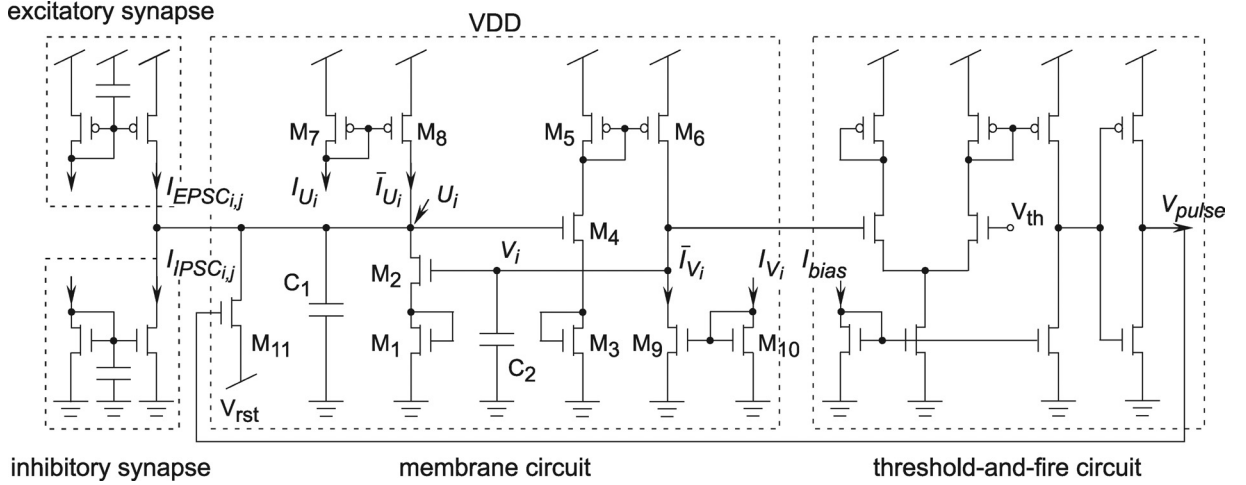are obtained. The resulting equations are suitable for analog integrated circuit implementation because of

Fig. 2. Schematic of the resonate-and-fire neuron circuit. The circuit consists of a membrane circuit, a threshold-and-fire circuit, and excitatory and inhibitory synaptic circuits. The membrane circuit has second-order dynamics containing two state variables U_i (a current-like variable) and V_i (a voltage-like variable), and shows oscillatory behavior mediated and modulated by a summation of synaptic inputs $I_{\text{in}} = \sum_j I_{\text{EPSC}_{i,j}} - \sum_j I_{\text{IPSC}_{i,j}}$.

(i) reducing the multiplication terms of the system variables of the original system, and (ii) exponential nonlinearity, which is an essential characteristic of semiconductor devices.[46]

3.1.2. Subthreshold current of MOS FETs

The current-voltage relationships of metal-oxide-semiconductor field-effect-transistors (MOS FETs) operating in the subthreshold region are described as follows:[1]

$$I_{ds,n} = SI_{n_o} \exp\left(\frac{\kappa_n V_g - V_s}{V_T}\right)$$
$$\times \left(1 - \exp\left(-\frac{V_d - V_s}{V_T}\right) + \frac{V_d - V_s}{V_{E,n}}\right) \quad (7)$$

$$I_{ds,p} = SI_{p_o} \exp\left(\frac{-\kappa_p V_g + V_s}{V_T}\right)$$
$$\times \left(1 - \exp\left(\frac{V_d - V_s}{V_T}\right) + \frac{V_s - V_d}{V_{E,p}}\right) \quad (8)$$

where $I_{ds,n}$ and $I_{ds,p}$ represent the currents of an nMOS and a pMOS FET, respectively, V_g, V_d and V_s the gate, drain, and source voltage, κ_n and κ_p the capacitive coupling ratio from the gate to channel, $V_T \equiv kT/q$ the thermal voltage (k: Boltzmann's constant, T: temperature, and q: electron charge), $V_{E,n}$ and $V_{E,p}$ the Early voltages, $S = W/L$ the aspect ratio of MOS FETs (W: the channel width and L:

the channel length), and I_{n_o} and I_{p_o} pre-exponential currents.[2]

When subthreshold MOS FETs are saturated ($V_d - V_s \geq 4V_T \approx 100\,\text{mV}$ at room temperature) and the Early voltages $V_{E,n}$ and $V_{E,p}$ are sufficiently larger than $|V_{ds}| = |V_d - V_s|$, (7) and (8) can be approximately rewritten as follows:

$$I_{ds,n} = SI_{n_o} \exp\left(\frac{\kappa_n V_g - V_s}{V_T}\right), \quad (9)$$

$$I_{ds,p} = SI_{p_o} \exp\left(\frac{-\kappa_p V_g + V_s}{V_T}\right). \quad (10)$$

Thus, the subthreshold currents of MOS FETs are exponential functions of input voltages.

3.1.3. Lotka-Volterra oscillator circuit

The LV system consisting of one predator and one prey is given in the following form:

$$\dot{z}_1 = z_1(r - z_2), \quad r > 0 \quad (11)$$
$$\dot{z}_2 = z_2(z_1 - 1) \quad (12)$$

where z_1 represents the prey population and z_2 the predator population, respectively, and r is a positive constant. This system has a conserved quantity:

$$c = z_1 + z_2 - \ln z_1 - r\ln z_2 \quad (13)$$

where c is a positive constant determined by initial conditions. Thus the LV system is a conservative system and has periodic solutions depending on the initial conditions.
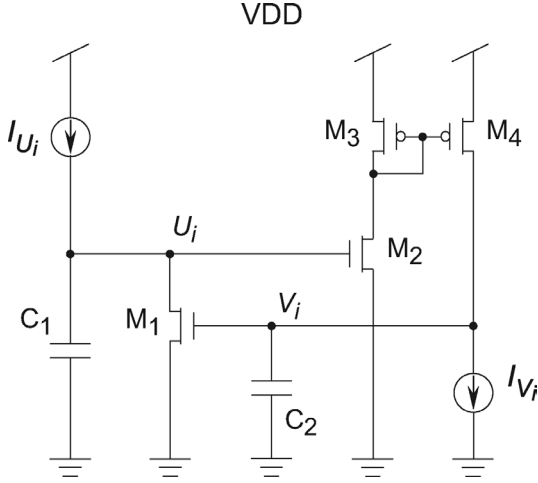
Fig. 3. Schematic of the Lotka-Volterra (LV) oscillator.

By applying the nonlinear transformation (5), (11) and (12) are transformed into:

$$\dot{x}_1 = r - b_2 \exp x_2 \qquad (14)$$

$$\dot{x}_2 = b_1 \exp x_1 - 1 \qquad (15)$$

where b_1 and b_2 represent scaling constants. Equations (14) and (15) can be implemented into silicon chips using the exponential current-voltage relationships described by (9) and (10).

Figure 3 shows the schematic of the LV oscillator circuit.[46] Applying Kirchhoff's current law at each node with capacitance in Fig. 3, we can obtain the following circuit dynamics:

$$C_1 \frac{dU_i}{dt} = I_{U_i} - SI_{n_o} \exp(\kappa_n V_i / V_T) \qquad (16)$$

$$C_2 \frac{dV_i}{dt} = SI_{n_o} \exp(\kappa_n U_i / V_T) - I_{V_i} \qquad (17)$$

where U_i and V_i represent the node voltages, C_1 and C_2 the capacitance, and I_{U_i} and I_{V_i} the bias current for a current mirror. When MOS FETs contained in the LV oscillator circuit operate under saturation, the circuit becomes a conservative system, and thus shows oscillations depending on initial conditions.

3.1.4. *Dynamics of membrane circuit*

We designed the membrane circuit by introducing dissipation terms and diode-connected transistors

into the LV oscillator circuit, as shown in Fig. 2. The dynamics of the membrane circuit is described as follows:

$$C_1 \frac{dU_i}{dt} = -g(U_i - V_{\mathrm{rst}}) + I_{in} + \bar{I}_{U_i}$$

$$- SI_{n_o} \exp\left(\frac{\kappa_n^2}{\kappa_n + 1} \frac{V_i}{V_T}\right) \qquad (18)$$

$$C_2 \frac{dV_i}{dt} = SI_{n_o} \exp\left(\frac{\kappa_n^2}{\kappa_n + 1} \frac{U_i}{V_T}\right) - \bar{I}_{V_i} \qquad (19)$$

where U_i and V_i represent the state variables, C_1 and C_2 the capacitance, g the conductance for the transistor M_{11}, V_{rst} the reset voltage, and I_{in} the summation of the synaptic currents:

$$I_{\mathrm{in}} = \sum_j I_{\mathrm{EPSC}_{i,j}} - \sum_j I_{\mathrm{IPSC}_{i,j}} \qquad (20)$$

where $I_{\mathrm{EPSC}_{i,j}}$ and $I_{\mathrm{IPSC}_{i,j}}$ represent the i-th postsynaptic currents through the jth excitatory and inhibitory synaptic circuits, respectively. Currents, $\bar{I}_{U_i}$ and $\bar{I}_{V_i}$ are described as follows:

$$\bar{I}_{U_i} = \alpha I_{U_i} \left(1 + \frac{\mathrm{VDD} - U_i}{V_{E,p}}\right) \qquad (21)$$

$$\bar{I}_{V_i} = \beta I_{V_i} \left(1 + \frac{V_i}{V_{E,n}}\right) \qquad (22)$$

where I_{U_i} and I_{V_i} represent the bias currents for the current mirror, VDD the power-supply voltage, and α and β the dimensionless constants:

$$\alpha = \left(1 + \frac{\mathrm{VDD} - V_{g1}}{V_{E,p}}\right)^{-1} \qquad (23)$$

$$\beta = \left(1 + \frac{V_{g2}}{V_{E,n}}\right)^{-1} \qquad (24)$$

where V_{g1} and V_{g2} represent the gate voltages of M_7–M_8 and M_9-M_{10}, which are determined by the bias currents I_{U_i} and I_{V_i}. As a result of introducing (21) and (22), the membrane circuit becomes a dissipative system.

The equilibrium point of the membrane circuit, (U_o, V_o), can easily be calculated, and the stability of the point can be analyzed by the eigenvalues of the

Jacobian matrix of the membrane circuit,

$$J = \begin{bmatrix} -\dfrac{\alpha I_{U_i}}{V_{E,p}} & -\dfrac{\kappa_n^2}{\kappa_n+1}\dfrac{I_{V_o}}{V_T} \\[3ex] \dfrac{\kappa_n^2}{\kappa_n+1}\dfrac{I_{U_o}}{V_T} & -\dfrac{\beta I_{V_i}}{V_{E,n}} \end{bmatrix} \quad (25)$$

$$= \begin{bmatrix} -\dfrac{I_{U_i}}{V_{E,p}+\mathrm{VDD}-V_{g1}} & -\dfrac{\kappa_n^2}{\kappa_n+1}\dfrac{I_{V_o}}{V_T} \\[3ex] \dfrac{\kappa_n^2}{\kappa_n+1}\dfrac{I_{U_o}}{V_T} & -\dfrac{I_{V_i}}{V_{E,n}+V_{g2}} \end{bmatrix}$$
$$(26)$$

where I_{U_o} and I_{V_o} represent the equilibrium current at the equilibrium point. It is assumed that the leak conductance g is zero. We used diode-connected transistors M_1 and M_3 to obtain small coefficients for I_{U_o} and I_{V_o}, and short transistors that have small Early voltages for M_7–M_{10} to obtain large coefficients for I_{U_i} and I_{V_i}. Consequently, the equilibrium point becomes a focus, and the membrane circuit exhibits damped oscillation in response to an input. In this case, the circuit dynamics is qualitatively equivalent to the membrane dynamics of the RFN model near the equilibrium point.

3.2.   *Threshold-and-fire circuit*

The threshold-and-fire circuit was constructed using a comparator circuit and an inverter. When input voltage V_i increases or decreases monotonously, the circuit generates output voltage V_{pulse}, which can be approximately described as follows:

$$V_{pulse} = \begin{cases} \mathrm{VDD} & V_i \geq V_{\mathrm{th}} + \delta V_{\mathrm{th}}, & (27) \\ \mathrm{GND} & \text{otherwise.} & (28) \end{cases}$$

where VDD represents a power-supply voltage, and GND a ground voltage. Effective threshold voltage is divided into a bias voltage for the comparator, V_{th}, and a time-dependent hysteresis voltage δV_{th}, which is approximately described as follows:

$$\delta V_{\mathrm{th}} = \int_0^T \frac{dV_i}{dt}dt \quad (29)$$

where T is an elapsed time since the voltage V_i has passed over the bias voltage V_{th}, which is described as follows:

$$T = \begin{cases} \dfrac{C_{\mathrm{inv}}}{I_{bias}} \cdot (\mathrm{VDD}-V_{\mathrm{inv}}) & \dfrac{dV_i}{dt} > 0, & (30) \\[3ex] \dfrac{C_{\mathrm{inv}}}{I_{bias}} \cdot V_{\mathrm{inv}} & \dfrac{dV_i}{dt} < 0. & (31) \end{cases}$$

where C_{inv} and V_{inv} represent an input capacitance and a reversal voltage of the inverter, respectively, and I_{bias} is a bias current for the comparator. In short, the threshold-and-fire circuit has hysteresis due to charging or discharging the input capacitance of the inverter.

3.3.   *Resonate-and-fire neuron circuit*

We here describe behavior of the RFN circuit. Pulse currents through excitatory or inhibitory synaptic circuits change the voltage U_i instantaneously and the trajectory of voltage oscillation of the membrane circuit is disturbed. If V_i exceeds a threshold voltage V_{th}, the threshold-and-fire circuit generates a spike (a pulse voltage V_{pulse}) after a slight delay, which is described by (30). Consequently, the transistor M_{11} turns on state, and then U_i is reset to the bias voltage V_{rst} instantaneously. As a result of resetting U_i, V_i decreases monotonously. Due to the time-dependent hysteresis described by (31), weak noise and jitters around V_{th} may not disturb threshold detection of the RFN circuit. After that, V_i decreases, and V_{pulse} is returned to 0. Therefore, the width of V_{pulse} is brief C and the RFN circuit seems to fire a spike. It can be said that such behavior of the RFN circuit is qualitatively the same as that of the RFN model.

4.   Results

We verified the performance of signal detection of the RFN circuit with SPICE simulations. We used the circuit simulator, T-Spice Pro, and the model parameters of the BSIM 3v3 LEVEL 49 model for the AMI 0.35μm CMOS process.

Through the following simulations, the supply voltages were set at VDD = 1.5 V, $V_{\mathrm{th}} = 850$ mV, and $V_{\mathrm{rst}} = 750$ mV, the bias currents were set at $I_{U_i} = I_{V_i} = 10$ nA, and $I_{\mathrm{bias}} = 250$ nA, and the capacitance were set at $C_1 = C_2 = 1.2$ pF. We used pulse currents (width: 0.3 μsec) as synaptic inputs, and the capacitance for excitatory and inhibitory synaptic circuits were set at $C_{\mathrm{p}} = 0.02$ pF.

4.1.   *Response to excitatory inputs*

Figure 4 shows typical behavior of the RFN circuit in response to excitatory synaptic inputs. When a pulse current (EPSC, amplitude: 300 nA) that could
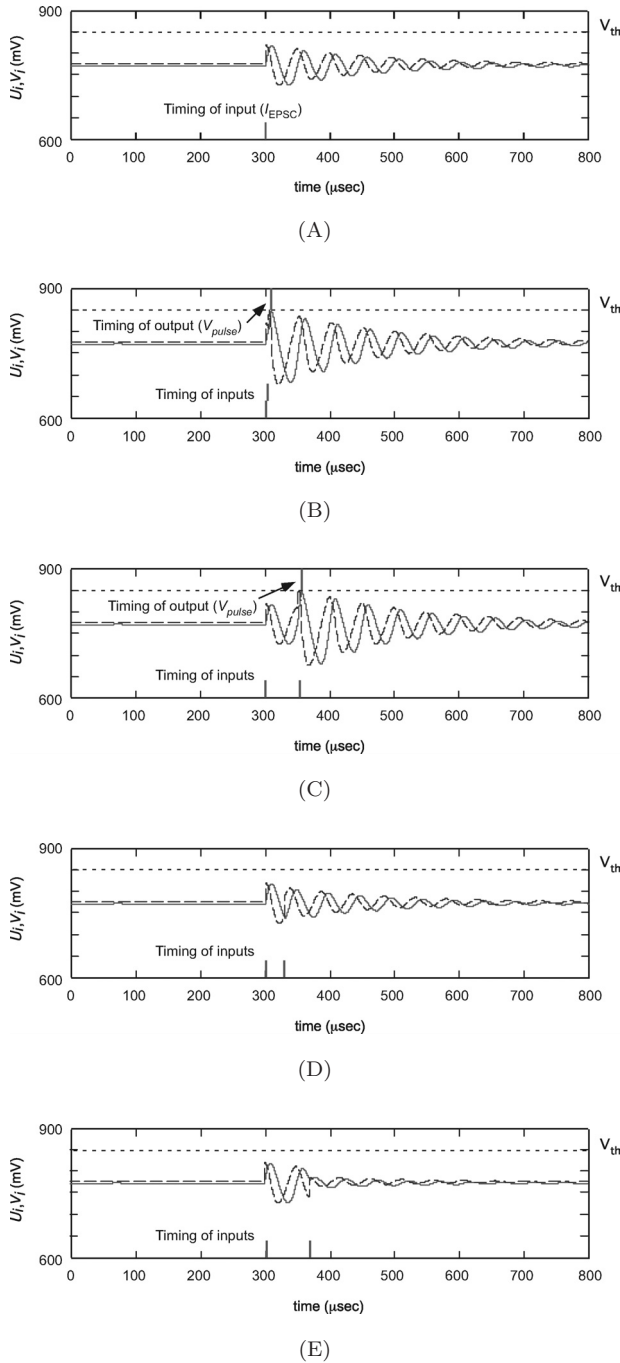
(A)

(B)

(C)

(D)

(E)

Fig. 4.   Responses to excitatory synaptic inputs, where solid and dashed lines represent V_i and U_i, respectively.

not make the voltage V_i exceeded the threshold voltage V_{th} was fed into the circuit, a damped oscillation of the voltages U_i and V_i occurred, in which the period of the oscillation was about $50\,\mu s$ (Fig. 4A). When a pair of pulses (EPSCs) with an interpulse-interval (IPI) in the range of 0 to $8.5\,\mu s$ was given
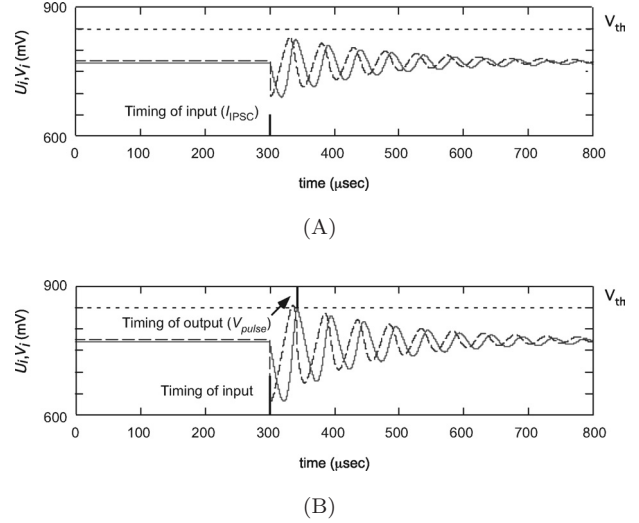

(A)

(B)

Fig. 5.   Responses to inhibitory synaptic inputs, where solid and dashed lines represent V_i and U_i, respectively.

into the RFN circuit, V_i exceeded V_{th} and the RFN circuit generated a pulse voltage V_{pulse}, and then U_i was reset to the bias voltage V_{rst} instantaneously. Thus, the RFN circuit seemed to fire a spike simply. Figure 4B shows a response to a pair of pulses with an IPI of $5\,\mu s$. When we gave two pulses with an IPI in the range of 45 to $55\,\mu s$ around the resonance interval of the RFN circuit, the RFN circuit also generated V_{pulse}. Figure 4C shows a response to a pair of pulses with the IPI of $50\,\mu s$. However, the RFN circuit did not fire a spike when the IPI was in other ranges, e.g. $30\,\mu s$ (Fig. 4D) and $70\,\mu s$ (Fig. 4E).

These results indicate that the RFN circuit can act as a coincidence detector and a bandpass filter for sequences of input pulses.

4.2.   *Response to inhibitory inputs*

Figure 5 shows typical behavior of the RFN circuit in response to inhibitory synaptic inputs. When an inhibitory pulse current (IPSC, amplitude: $-500\,nA$) was given into the circuit, a damped subthreshold oscillation of U_i and V_i occurred as well as when an excitatory pulse was given (Fig. 5A). The amplitude of the oscillation increased with the amplitude of the inhibitory synaptic input. When a strong inhibitory pulse (amplitude: $-900\,nA$) was given, V_i exceeded V_{th} as a result of a rebound effect of the inhibitory input, as shown in Fig. 5B. Thus, the RFN circuit generated V_{pulse} and U_i was reset to V_{rst} after a slight delay. These results are indicative of the

property of the post-inhibitory rebound of the RFN circuit.

4.3.   *Effects of additive white noise*

We here consider the effects of white noise on the circuit operation. It is suggested that a weak noisy input induces a sustained subthreshold oscillation in the RFN model.[51] When we give a weak noisy input $\epsilon I(t)$ into the RFN model as described as follows:

$$\dot{z} = (-\epsilon + iw)z + \epsilon I(t) \qquad (32)$$

the noisy input induces a sustained oscillation, which is described as follows:

$$z = I^*(w)\exp(iwt) \qquad (33)$$

where $I^*(w)$ represents the Fourier coefficient of the $I(t)$ corresponding to the frequency w, and $|I^*(w)|$ the average amplitude of the oscillation, as proven by Izhikevich.[51] As in the case of the RFN model, weak noise induces a sustained subthreshold oscillation in the RFN circuit. If white noise in the RFN circuit, which has little effect on the equilibrium point and its stability, the average amplitude of the oscillation can be estimated in a similar way to (32) and (33). The average frequency of the oscillation is nearly equal to the natural frequency of the RFN circuit since the power spectrum of the white noise is frequency independent.

Although the white noise induces the fluctuation of the voltages U_i and V_i, such fluctuation may not affect the operation of the threshold-and-fire circuit due to the time-dependent hysteresis described in Sec. 3.2. Thus, the RFN circuit can operate correctly even in the presence of the white noise.

4.4.   *Effects of background random activity*

We then consider the effects of background random activity on the performance of the signal detection in the RFN circuit. We employed a sequence of random pulses as background activity. The IPI distribution is Gaussian, the ratio of the standard deviation to the mean of IPI is 0.1, and the amplitude of pulses are $60\,\mathrm{nA}$ for excitation and $-60\,\mathrm{nA}$ for inhibition,
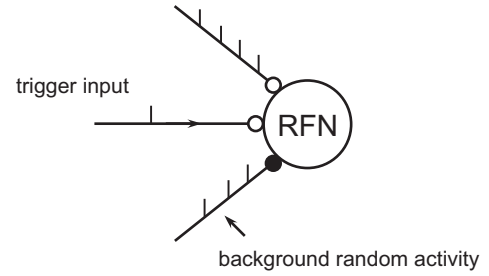

Fig. 6.   RFN circuit under the influence of background random activity. Open and closed circles are excitatory and inhibitory synaptic circuits, respectively.

respectively (Fig. 6). It should be noted that such random activity can be regarded as strong noise.

4.4.1.   *Resonance interval modulation*

We investigated resonance interval modulation of the RFN circuit under the influence of the background random activity. The resonance interval of the RFN circuit decreased with increase in the mean IPI of the inhibitory random activity, and increased with increase in the mean IPI of the excitatory random activity, as shown in Fig. 7. This is because the excitatory random activity increases the equilibrium voltages (U_o, V_o), and then the equilibrium currents (I_{U_o}, I_{V_o}), that is the RFN circuit is depolarized. In contrast to the excitation, the inhibitory background activity decreases the equilibrium voltages, and then the equilibrium currents, that is the RFN circuit is hyperpolarized. As shown in the Jacobian matrix (26), the frequency of the subthreshold oscillation depends on the equilibrium currents, and thus the resonance interval changes.
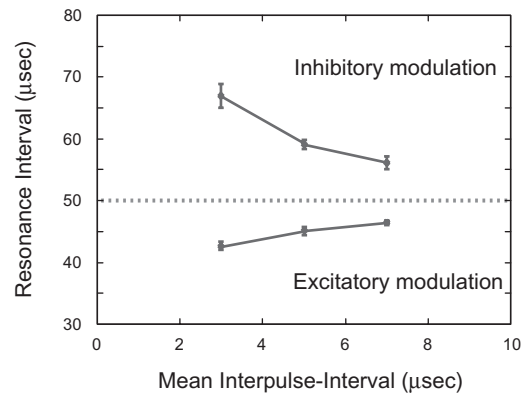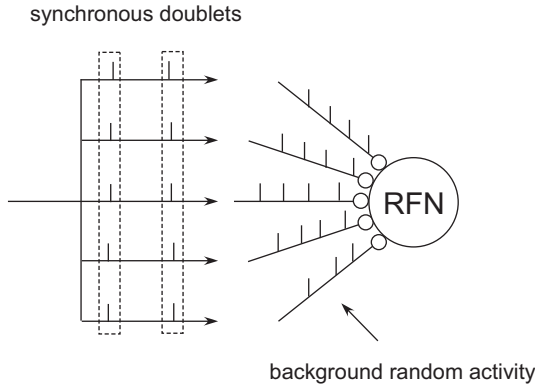

Fig. 7.   Resonance Interval Modulation.

synchronous doublets

Fig. 8. RFN circuit with five excitatory synaptic circuits, in which each carries synchronous doublets embedded in background random activity.

(A)

(B)

Fig. 9. Coincidence detection of synchronous doublets embedded in background random activity.

4.4.2. *Robustness of frequency preference*

We here describe how background random activity affects the performance of the frequency preference of the RFN circuit. We consider an RFN circuit with five excitatory synaptic circuits, each of which carries random pulses (the mean of IPI: $25\,\mu$s) as background activity, and synchronous doublets to the RFN circuit, as shown in Fig. 8.

The RFN circuit can detect synchronous doublets with the resonance interval embedded in background random pulses. If the mean of IPI of the background pulses is smaller than the resonance interval of the RFN circuit, the background pulses are filtered due to the band-pass characteristics of the RFN circuit. Furthermore, if the mean interval of the synchronous doublets is nearly equal to the resonance frequency modulated by the background random activity, the synchronous doublets can be detected. Figure 9 shows that the RFN circuit can be resonance with synchronous doublets given at about $300\,\mu$s and $350\,\mu$s even in the presence of the weak subthreshold oscillation mediated by the the background random activity.

4.5. *Influence of device mismatch*

We further consider the influence of device mismatch on the circuit properties of the RFN circuit. The device mismatch may mainly affects the properties of the membrane circuit. We assumed the variation of threshold voltage of transistors, ΔV_{TH}, as device mismatch, and evaluated how such variation
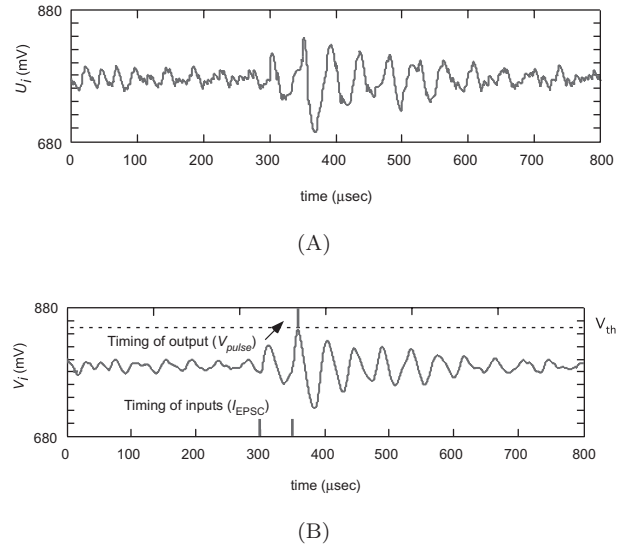
spreads the equilibrium voltages and resonance interval of the membrane circuit using Monte-Carlo simulations. Focusing on symmetry in the membrane circuit (Fig. 2), we only considered the local variation of the transistors comprising the membrane circuit, and set the standard deviation of the threshold voltage V_{TH} between a pair of transistors (e.g. M1 and M3, and M5 and M6), $\sigma(V_{\text{TH}}) = 1$ mV. Figure 10 shows the statical distribution of the equilibrium voltages U_o and V_o. One of the influence of the variation of the equilibrium voltages is on the variation of distance between the equilibrium voltage V_o and the threshold voltage of the threshold-and-fire circuit, V_{th}. This influence can be reduced by tuning the ratio of the variation and the distance. Another influence is on the variation of the resonance interval, as shown in Fig. 11. The ratio between the mean and standard deviation of the resonance interval was calculated at 2.3%, and thus such influence may be not critical for the frequency preference of the RFN circuit.

The influence of the device mismatch considered here can also be reduced by enlarging the size of the transistors comprising the RFN circuit. In addition, MOS transistor scaling supports this approach since the device mismatch of MOS transistors is generally proportional to the oxide thickness, which decreases with the scaling. The influence of device mismatch may decrease with decreasing the oxide thickness due to the MOS transistor scaling if the size of the RFN circuit is constant. We can also estimate the local
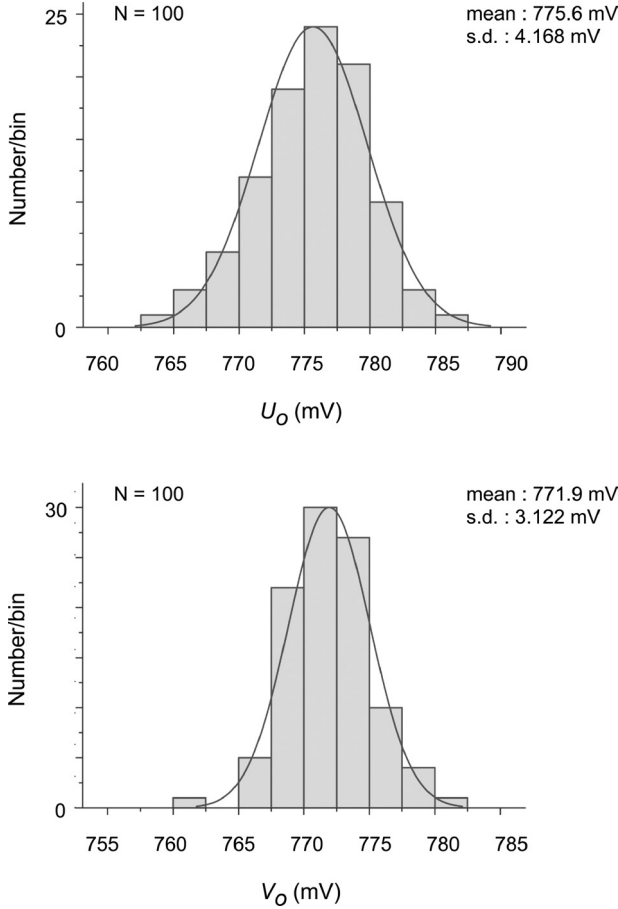
Fig. 10.   Statical distribution of equilibrium voltages.

Fig. 11.   Statical distribution of resonance interval.

variation of device parameters as the oxide thickness and the size of transistors are given. For instance, the local variation of the threshold voltage can be estimated as follows:

$$\sigma(V_{\text{TH}}) \approx A_{\text{TH}} \frac{t_{ox}}{\sqrt{LW}} \qquad (34)$$

where t_{ox} represents the oxide thickness, L and W the channel width and length, respectively, and $A_{\text{TH}} = 1\,\text{V}$ a proportional constant at a standard process. We assumed the oxide thickness $t_{ox} = 8.0$ nm in the Monte-Carlo simulations. Thus, if we want to obtain $\sigma(V_{\text{TH}}) = 1\,\text{mV}$, the area of a transistor should be more than $LW = 64\ \mu\text{m}^2$.

4.6.   *Estimated power consumption*

The power consumption of the RFN circuit at a steady state can be calculated as follows:

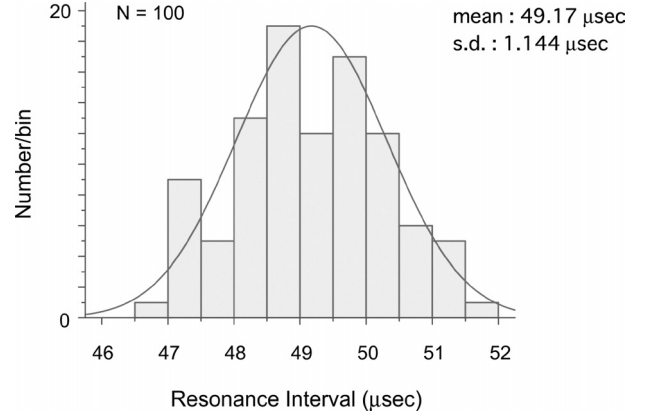$$P = \text{VDD} \cdot (I_{U_o} + 2I_{V_o} + I_{U_i} + I_{V_i} + 3I_{bias}) \quad (35)$$

where I_{U_o} and I_{V_o} represent the equilibrium currents of the membrane circuit, I_{U_i} and I_{V_i} the bias currents for the membrane circuit, and I_{bias} the bias current for the threshold-and-fire circuit. By assuming the same parameters as used in the previous simulations, we measured the currents as follows: $I_{U_o} = 11.8\,\text{nA}$, $I_{V_o} = 12.8\,\text{nA}$, $I_{U_i} = I_{V_i} = 10\,\text{nA}$, and $I_{bias} = 500\,\text{nA}$. Thus, the power consumption was estimated at $2.34\,\mu\text{W}$.

5.   Summary and Concluding Remarks

In this paper, we have proposed analog integrated circuit implementation of a resonate-and-fire neuron (RFN) model. The RFN circuit has been derived from the Lotka-Volterra (LV) oscillator circuit to mimic the dynamical behavior of the RFN model: the damped subthreshold oscillation, resulting into the coincidence detection, frequency preference, and post-inhibitory rebound. Due to such properties, the RFN circuit can act as a coincidence detector, and at the same time as a band-pass filter for a spike sequence even in the presence of the additive white noise and the background random activity. We have also considered the influence of the device mismatch on the circuit properties of the RFN circuit. Such influence can be reduced by enlarging the size of the RFN circuit, and the scaling of MOS transistors is suitable for this approach. The typical operating time-scales we used here are in the order of tens of microseconds. Therefore, our circuit is insufficient for dealing with natural signals in speech and visual processing, in which time scales are in the order of milliseconds. Our circuit would be applied to high-order

neuromorphic processing using the event-based computation, concerned with associative memory[30] and sequential coding.[34]

In addition, Izhikevich has recently suggested in his literature that biological neurons are classified into two categories; integrator and resonators.[51] It is interesting to reflect that cortical neurons act as integrators or resonators depending on whether they are excitatory or inhibitory, respectively. This fact implies that integrators and resonators in biological neural network have a possibility to share roles in information processing with each other. In a similar way, the RFN circuit plays a complementary role to IFN circuits. Thus, the RFN circuit is a candidate as essential component for large-scale integration of functional networks of silicon spiking neurons.

References

1. C. A. Mead, *Analog VLSI and Neural Systems* (Addison-Wesley, Reading, 1989).

2. S.-C. Liu, J. Kramer, G. Indiveri, T. Delbruck and R. Douglas, *Analog VLSI: Circuits and Principles* (MIT Press, 2002).

3. W. Maass and C. M. Bishop (ed.), *Pulsed Neural Networks* (MIT Press, 1998).

4. T. Fukai, Competition in the temporal domain among neural activities phase-locked to subthreshold oscillations, *Biol. Cybern.* **75** (1996) 453–461.

5. M. Hanagata, Y. Horio and K. Aihara, Asynchronous pulse neural network model for VLSI implementation, *IEICE Trans. Fund.* **E81-A**(9) (1998) 1853–1859.

6. W. Senn, I. Segev and M. Tsodyks, Reading neuronal synchrony with depressing synapses, *Neural Computation* **10**(4) (1998) 815–819.

7. D. J. Mar, C. C. Chow, W. Gerstner, R. W. Adams and J. J. Collins, Noise shaping in populations of coupled model neurons, in *Proc. Natl. Acad. Sci.* **96**(18) (1999) 10450–10455.

8. F. Wörgötter, A. Cozzi and V. Gerdes, A parallel noise-robust algorithm to recover depth information from radial flow fields, *Neural Computation* **11** (1999) 381–416.

9. S. Fusi and M. Mattia, Collective behavior of networks with linear (VLSI) Integrate and Fire Neurons, *Neural Computation* **11** (1999) 633–652.

10. S. Fusi, M. Annunziato, D. Badoni, A. Salamon and D. J. Amit, Spike-driven synaptic plasticity: Theory, simulation, VLSI implementation, *Neural Computation* **12** (2000) 2227–2258.

11. T. Fukai and S. Kanemura, Noise-tolerant stimulus discrimination by synchronization with depressing synapses, *Biol. Cybern.* **85** (2001) 107–116.

12. G. Bugmann, Synaptic depression increases the selectivity of a neuron to its preferred pattern and binarizes the neural code, *Biosystems* **67** (2002) 17–26.

13. R. Reeve and B. Webb, New neural networks for robot phonotaxis, *Philos. Trans. A Math. Phys. Eng. Sci.* **361** (2003) 2245–2266.

14. J. J. Hopfield and C. D. Brody, Learning rules and network repair in spike-timing-based computational networks, in *Proc. Nacl. Acad. Sci.* **101**(1) (2004) 337–342.

15. M. Mahowald, *An Analog VLSI System for Stereoscopic Vision* (Boston, MA: Kluwer Academic Publishers, 1994).

16. F. Tenore, R. Etienne-Cummings and M. A. Lewis, A programmable array of silicon neurons for the control of legged locomotion, in *Proc. IEEE Int. Symp. Circ. Syst.* (2003).

17. D. H. Goldberg, G. Cauwenberghs and A. G. Andreou, Probabilistic synaptic weighting in a reconfigurable network of VLSI integrate-and-fire neurons, *Neural Networks* **14**(6–7) (2001) 781–793.

18. S.-C. Liu, J. Kramer, G. Indiveri, T. Delbruck, T. Burg and R. J. Douglas, Orientation-selective aVLSI spiking neurons, *Neural Networks* **14**(6–7) (2001) 629–643.

19. E. Culurciello, R. Etienne-Cummings and K. Boahen, A biomorphic digital image sensor, *IEEE Journal of Solid-State Circuits* **8**(2) (2003) 281–294.

20. D. C. Ng, K. Isakari, A. Uehara, K. Kagawa, T. Tokuda, J. Ohta and M. Nunoshita, A study of bending effect on pulsed frequency modulation based photosensor for retinal prosthesis, *Jpn. J. Appl. Phys.* **42**(12) (2003) 7621–7624.

21. T. Y. W. Choi, B. E. Shi and K. A. Boahen, An ON-OFF orientation selective address event representation image transceiver chip, *IEEE Trans. Circ. Sys.-I* **51**(2) (2004) 342–353.

22. R. J. Vogelstein, U. Mallik, G. Cauwenberghs, E. Culurciello and R. Etienne-Cummings, Saliency-driven image acuity modulation on a reconfigurable silicon array of spiking neurons, *Adv. Neural Info. Proc. Syst.* **16** (2005).

23. A. Linares-Barranco, G. Jimenez-Moreno, B. Linares-Barranco and A. Civit-Ballcels, On algorithmic rate-coded AER generation, *IEEE Trans. on Neural Networks* in printing.

24. N. Kumer, W. Himmelbauer, G. Cauwenbeghs and A. Andreou, An analog VLSI chip with asynchronous interface for auditory feature extraction, *IEEE Trans. Circ. Sys.-II* **45**(5) (1998) 600–606.

25. M. Cheely and T. Horiuchi, Analog VLSI models of range-tuned neurons in the bat echolocation system, *EURASIP J. Appl. Signal Proc.* **7** (2003) 649–658.

26. R. Reeve, B. Webb, A. Horchler, G. Indiveri and R. Quinn, New technologies for testing a model of cricket phonotaxis on an outdoor robot platform, *Robotics and Autonomous Systems* **51**(1) (2005) 41–54.

27. A. Van Schaik and S.-C. Liu, AER EAR: A matched silicon cochlea pair with address event representation interface, in *Proc. IEEE Int. Symp. on Circ. and Syst.* Kobe, Japan, May **V** (2005) 4213–4216.

28. S.-C. Liu and R. J. Douglas, Temporal coding in a network of silicon integrate-and-fire neurons, *IEEE Trans. Neural Networks* **15**(5) (2004) 1305–1314.

29. Y. Kanazawa, T. Asai, M. Ikebe and Y. Amemiya, A novel CMOS circuit for depressing synapse and its application to contrast-invariant pattern classification and synchrony detection, *Int. J. Robotics and Automation* **19**(4) (2004) 206–212.

30. H. Tanaka, T. Morie and K. Aihara, Associative memory operation in a Hopfield-type spiking neural network with modulation of resting membrane potential, presented at *Int. Symp. on Nonlinear Theory and its Applications*, Bruges, Belgium (2005).

31. G. Indiveri, E. Chicca and R. J. Douglas, A VLSI array of low-power spiking neurons and bistable synapse with spike-timing dependent plasticity, *IEEE Trans. Neural Networks*, to be appeared.

32. D. Muir, G. Indiveri and R. Douglas, Form specifies function: Robust spike-based computation in analog VLSI without precise synaptic weights, in *Proc. the IEEE Int. Sympo. Circ. and Syst.*, Kobe, Japan (May 2005).

33. A. Utagawa, T. Asai, T. Hirose and Y. Amemiya, A neuromorphic LSI performing noise-shaping pulse-density modulation with ultralow-power subthreshold neuron circuits, *10th International Conference on Cognitive and Neural Systems*, Boston, USA (May 2006).

34. J. V. Arthur and K. Boahen, Learning in silicon: Timing is everything, *Adv. Neural Info. Proc. Syst.* **17** (2006).

35. C. Rasche and R. H. R. Hahnloser, Silicon synaptic depression, *Biol. Cybern.* **84** (2001) 57–62.

36. S.-C. Liu, Analog VLSI circuits for short-term dynamic synapses, *EURASIP J. Appl. Signal Proc.* **7** (2003) 620–628.

37. R. Z. Shi and T. Horiuchi, A summating, exponentially-decaying CMOS synapse for spiking neural systems, *Adv. Neural Info. Proc. Syst.* **16** (2004).

38. R. J. Vogelstein, F. Tenore, R. Philip, M. S. Adlerstein, D. H. Goldberg and G. Cauwenberghs, Spike timing-dependent plasticity in the address domain, *Adv. Neural Info. Proc. Syst.* **15** (2003).

39. A. Bofill-i-Petit and A. F. Murray, Synchrony detection and amplification by silicon neurons with STDP synapses, *IEEE Trans. Neural Networks* **15**(5) (2004) 1296–1304.

40. K. Cameron, V. Boonsobhak, A. Murray and D. Ranshaw, Spike timing dependent plasticity (STDP) can ameliorate process variations in neuromorphic systems, *IEEE Trans. Neural Networks* **16**(6) (2005) 1626–1637.

41. G. M. Tovar, T. Hirose, T. Asai and Y. Amemiya, Precisely-timed synchronization among spiking neural circuits on analog VLSIs, in *Proc. the 2006 RISP International Workshop on Nonlinear Circuits amd Signal Processing* Honolulu, USA (March 2006), pp. 62–65.

42. S. R. Schultz and M. A. Jabri, Analogue VLSI integrate-and-fire neuron with frequency adaptation, *Electronic Letters* **31**(16) (1995) 1357–1358.

43. K. A. Boahen, *Retinomorphic Vision Systems*: *Reverse Engineering the Vertebrate Retina*, Ph.D. Thesis, California Institute of Technology, Pasadena CA (1997).

44. A. Van Schaik, Building blocks for electronic spiking neural networks, *Neural Networks* **14**(6–7) (2001) 617–628.

45. S.-C. Liu and B. A. Minch, Homeostasis in a silicon integrate-and-fire neuron, *Adv. Neural Info. Proc. Syst.* **13** (2001).

46. T. Asai, Y. Kanazawa and Y. Amemiya, A subthreshold MOS neuron circuit based on the Volterra system, *IEEE Trans. Neural Networks* **14**(5) (2003) 1308–1312.

47. H. Nakano and T. Saito, Grouping synchronization in a pulse-coupled network of chaotic spiking oscillators, *IEEE Trans. Neural Networks* **15**(5) (2004) 1018–1026.

48. Y. Horio, T. Taniguchi and K. Aihara, An asynchronous spiking chaotic neuron integrated circuit, *Neurocomputing* **64** (2005) 447–472.

49. K. Nakada, T. Asai and H. Hayashi, A silicon resonate-and-fire neuron based on the Volterra system, in *Proc. the 2005 International Symposium on Nonlinear Theory and Its Applications,* 82–85, Bruges, Belgium (2005).

50. E. M. Izhikevich, Resonate-and-fire neurons, *Neural Networks* **14** (2001) 883–894.

51. E. M. Izhikevich, *Dynamical Systems in Neuroscience*: *The Geometry of Excitability and Bursting* (The MIT press, 2006).

52. M. J. M. Pelgrom, A. C. J. Duinmaijer and A. P. G. Welbers, Matching properties of MOS transistors, *IEEE Journal of Soilid-State Circuits* **SC-24** (1989) 1433–1440.

53. S. N. Goel, C. S. Maitra and W. E. Montroll, On the Volterra and other nonlinear models of interacting populations, *Rev. Mod. Phys.* **43** (1971) 231–276.